catalysts

MDPI

Article

Nanostructured Fe-N-C as Bifunctional Catalysts for Oxygen Reduction and Hydrogen Evolution

Williane da Silva Freitas, Pedro Pablo Machado Pico, Alessandra D'Epifanio and Barbara Mecheri *

Department of Chemical Science and Technologies, University of Rome Tor Vergata, Via Della Ricerca Scientifica, 00133 Rome, Italy; williane.freitas@uniroma2.it (W.d.S.F.); pedro.pablo.machado.pico@uniroma2.it (P.P.M.P.); alessandra.d.epifanio@uniroma2.it (A.D.)

* Correspondence: barbara.mecheri@uniroma2.it; Tel.: +39-06-7259-4488

Abstract: The development of electrocatalysts for energy conversion and storage devices is of paramount importance to promote sustainable development. Among the different families of materials, catalysts based on transition metals supported on a nitrogen-containing carbon matrix have been found to be effective catalysts toward oxygen reduction reaction (ORR) and hydrogen evolution reaction (HER) with high potential to replace conventional precious metal-based catalysts. In this work, we developed a facile synthesis strategy to obtain a Fe-N-C bifunctional ORR/HER catalysts, involving wet impregnation and pyrolysis steps. Iron (II) acetate and imidazole were used as iron and nitrogen sources, respectively, and functionalized carbon black pearls were used as conductive support. The bifunctional performance of the Fe-N-C catalyst toward ORR and HER was investigated by cyclic voltammetry, rotating ring disk electrode experiments, and electrochemical impedance spectroscopy in alkaline environment. ORR onset potential and half-wave potential were 0.95 V and 0.86 V, respectively, indicating a competitive performance in comparison with the commercial platinum-based catalyst. In addition, Fe-N-C had also a good HER activity, with an overpotential of 478 mV @10 $mAcm^{-2}$ and Tafel slope of 133 $mVdec^{-1}$, demonstrating its activity as bifunctional catalyst in energy conversion and storage devices, such as alkaline microbial fuel cell and microbial electrolysis cells.

Keywords: PGM-free electrocatalysts; oxygen reduction; hydrogen evolution; energy conversion; bioelectrochemical systems

Citation: da Silva Freitas, W.; Machado Pico, P.P.; D'Epifanio, A.; Mecheri, B. Nanostructured Fe-N-C as Bifunctional Catalysts for Oxygen Reduction and Hydrogen Evolution. *Catalysts* **2021**, *11*, 1525. https://doi.org/10.3390/catal11121525

Academic Editor: David Sebastián

Received: 8 November 2021
Accepted: 10 December 2021
Published: 15 December 2021

1. Introduction

The environment pollution generated by use of fossil fuels combined with their depletion demands urgent development of renewable and clean energy technology. In this scenario, fuel cells and electrolyzers offer a good strategy for electrochemical energy storage and conversion; in particular microbial fuel cells are able to generate electricity by the oxidation of organic matter at the anode side promoted by the action of microorganisms [1–3]. Oxygen reduction reaction (ORR) and hydrogen evolution reaction (HER) are the most crucial cathodic reactions of fuel cell and electrolyzers, respectively. The development of bifunctional electrocatalyst materials plays a key role in the rapid advancement of these hydrogen-based renewable energy strategies [4].

The most used catalysts for ORR and HER are based Platinum Group Metals (PGM) [5,6], due to the sluggish kinetics of both reactions. However, low availability and high cost of PGM catalysts limits a commercial application for the MFC and electrolyzes devices, requiring low cost and earth abundant materials [5]. The development of catalysts based on PGM-free materials was indeed pursued by the electrocatalyst community, demonstrating that PGM-free catalysts can be an alternative to Pt due to their high activity in acid and alkaline environment and good durability towards both ORR and HER [1,7–13].

ORR proceeds through a 4-electron or a 2-electron mechanism [14]. Direct four-electron mechanism is the most efficient, since it allows obtaining a maximum energy from

the reaction and there is no hydrogen peroxide generation which contributes to the active sites deactivation [14–16]. Metal-Nitrogen-Carbon (M-N-C) materials have shown good catalytic performance for ORR [3,17–23].

Similar to ORR, HER activity has a pH dependence, and in alkaline environments the reaction rate is lower than in acidic environments [4,24,25]. This kinetic limitation in alkaline pH is due to the water dissociation step that delivers H^+ for the following reactions, which does not take place at acidic pH [26]. Regarding the reaction mechanism, the HER takes place via the Volmer−Heyrowsky or the Volmer−Tafel mechanisms, and for both mechanisms, the HER proceeds through the adsorption of H atoms at the electrode surface (H_{ads}) [27]. Although the higher activity of PGM and PGM-Free catalysts toward HER in acidic medium as compared to alkaline one, the low durability of those materials in acid-based fuel cells and electrolyzers under operating conditions is still a strong issue [6,28,29]. Thus, alkaline pH has been found to be a proper environment to achieve a good compromise between activity and durability of PGM-Free materials, under operating conditions of cathodes of fuel cells and electrolyzers.

Metal alloys and metal oxides/sulfides have shown catalytic activity for HER in alkaline environment; bimetallic alloys have been also considered as a good candidate due to the synergistic effect between adjacent atoms and a variation of the electronic density of state and M-H strength [30,31]. Metal oxides have the advantage of being easily synthesized, leading to chemical stability [32]. Metal sulfides are also considered as promising electrocatalysts due to its unique properties, high conductivity, high catalytic activity, high affinity for hydrogen adsorption, low cost, and availability [33–35]. In addition, M-N-C materials have received recent attention as catalysts for HER [36–38]. Tailoring texture of M-N-C materials can boost ORR and HER activity and mass transfer [39–42].

In this work, we developed a synthesis strategy to obtain a Fe-N-C bifunctional catalyst by wet impregnation and pyrolysis steps. Iron (II) acetate and imidazole were used as iron and nitrogen sources, respectively, and functionalized carbon black pearls were used as conductive support. The bifunctional performance of the Fe-N-C catalyst toward ORR and HER was investigated by cyclic voltammetry, rotating ring disk electrode experiments, and electrochemical impedance spectroscopy in alkaline environments.

2. Results and Discussion

Thermal properties of the carbon support, pristine metal- and nitrogen-containing precursors, and the Fe-N-C material before pyrolysis, were investigated by thermogravimetric analysis (TGA) (Figure 1a). A complete one-step decomposition (~1 wt.% at 800 °C) can be seen for imidazole, with onset and end-set temperatures of 147 °C and 205 °C, respectively, in agreement with the existing literature [43]. The TG curve of the carbon support indicates that BP exhibits a main first mass loss in the 30–115 °C temperature range due to the vaporization of adsorbed water molecules; mass losses above 120 °C were due to the decomposition of oxygenated functionalities in carbon black pearls [21]. Iron acetate also shows a first weight loss up to 120 °C due to the vaporization of adsorbed water molecules, while weight losses in the 120–300 °C can be ascribed to salt decomposition leading to formation of iron oxide [44]. TG curves of the Fe-N-C precursor show three main mass losses: the first is due to vaporization of adsorbed water molecules; the second is due to the decomposition of imidazole and iron salt, and the third one above 400 is due to the desorption of oxygen-groups in the carbon support matrix. As expected, the TG curve of the Fe-N-C precursor is different as compared to the pristine compounds, imidazole, iron acetate, and BP, in which the main mass loss from 138 to 316 °C (Table 1) indicates a higher contribution of imidazole carbonization, as can be evidenced by comparison of TG curves profiles for imidazole and iron acetate at this temperature range.

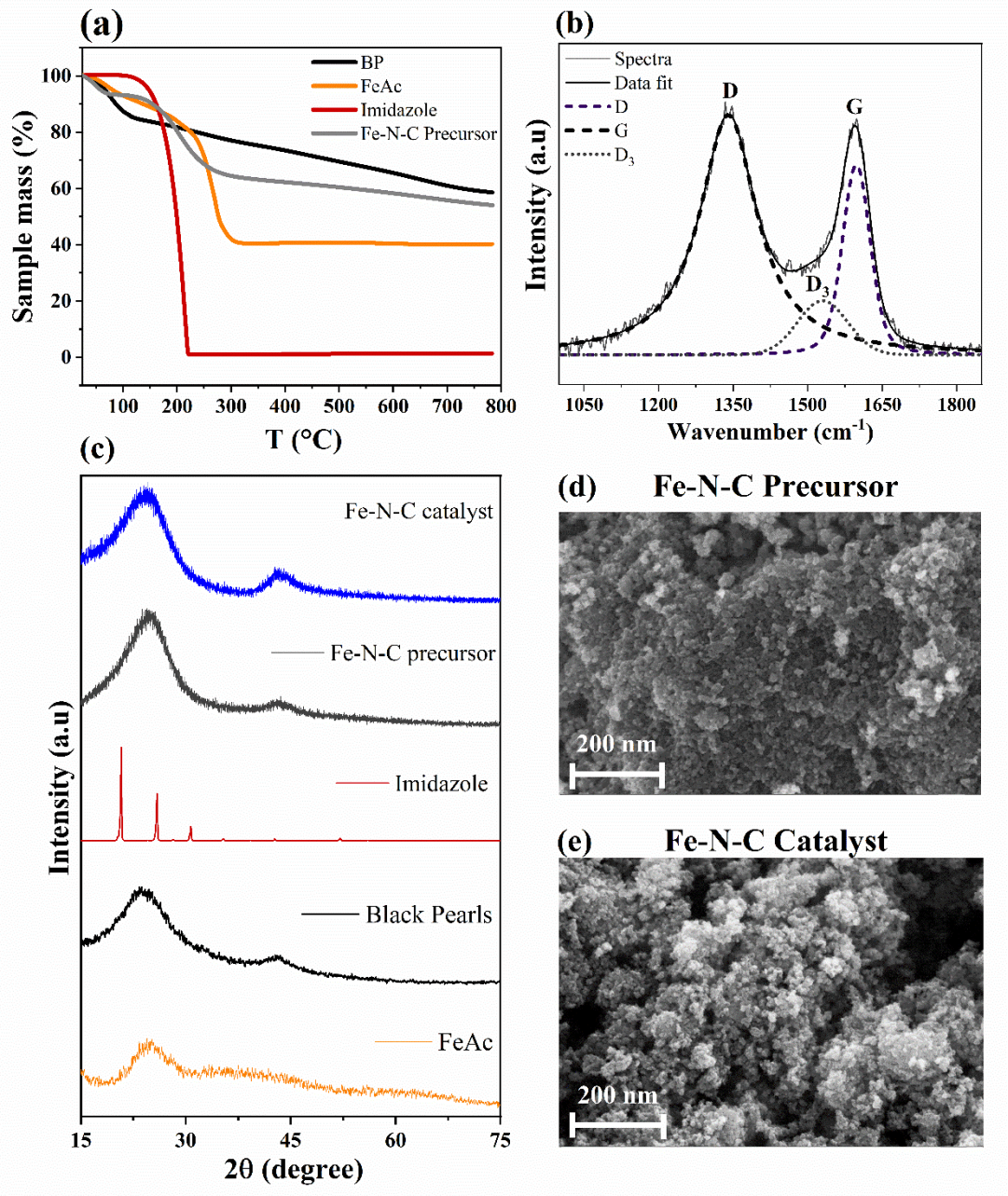

Figure 1. Thermogravimetric analysis of carbon black pearls, iron acetate, imidazole, and Fe-N-C precursor before pyrolysis treatment (**a**); Raman spectra and curve fitting of the Fe-N-C catalyst (**b**); XRD patterns for the Fe-N-C catalyst (Blue) and Fe-N-C precursor (Gray), imidazole (Red) carbon black pearls (Black), and iron acetate (Orange) (**c**) and, SEM image for the Fe-N-C materials before (**d**) and after (**e**) pyrolysis under ammonia atmosphere.

The Raman spectrum (Figure 1b) of Fe-N-C catalyst shows the G and D band: the first one is related to the E_{2g} mode of ordered graphitic carbon, while the second one is related to A1g vibrational mode from defects in the carbon matrix. The D_3 band is also observed, arising from interstitial defects of amorphous sp^2 carbon [45,46]. The ratio between the intensity of D and G bands (I_D/I_G) was 1.04, in good agreement with others metal/nitrogen-doped carbon catalysts reported in literature [47–50]. Such value is related to the density of functional groups in the carbon framework [51,52], confirming the role of nitrogen-containing precursor and ammonia atmosphere in the carbon matrix functionalization with iron and nitrogen functionalities.

Table 1. Temperature range (T_{Range}) and the corresponding mass loss (wt.%) from TG curves.

Parameter	Imidazole	FeAc	BP	Fe-N-C
Mass loss I				
T_{range} (°C)	147–224	68–135	44–117	33–75
Mass (wt.%)	98.6	8.2	15	6.5
Mass loss II	-			
T_{Range} (°C)	-	204–258	136–223	138–316
Mass (wt.%)	-	7.2	8	29.6
Mass loss III	-			
T_{Range} (°C)	-	261–369	324–744	324–755
Mass (wt.%)	-	38	17	9.30
Residual mass (wt.%)	1.4	39.2	59	55

Figure 1c shows XRD patterns of Fe-N-C material before and after pyrolysis in ammonia atmosphere and XRD pattern of the pristine carbon support, metal-, and nitrogen-containing precursors. The diffractogram for imidazole shows well-defined and intense peaks in the 2θ range 10–30°, in good agreement with the reference diffraction pattern (22–1759 in the ICDD database). For BP, two peaks at 2θ = 23.8° and 43° are observed, corresponding to (002) and (101) diffractions of graphitic carbon, respectively [53]. The peak at 2θ = 25° corresponding to (002) diffraction of graphitic carbon can be seen also for iron acetate as a contribution of the acetate anion. The diffraction pattern for the Fe-N-C precursor before pyrolysis shows the typical peaks of graphitic carbon from the BP matrix. This profile is also evident in the pattern of the pyrolyzed material, after complete iron and nitrogen-based precursors graphitization. No peaks related to the presence of iron oxides or carbides, suggesting a good interaction of the metal- and nitrogen-containing precursors in the formation of M-N-C active sites. SEM images (Figure 1d,e) indicated a porous structure for both samples before and after pyrolysis. Additionally, SEM images indicates that the heat treatment in ammonia atmosphere preserves the morphology of the Fe-N-C precursor. As previously found for similar materials [54], the surface area slightly increased after pyrolysis in ammonia, as confirmed by electrochemical surface area (ECSA) values which increased from 806 m^2g^{-1} (non-pyrolyzed material) to 875 m^2g^{-1} (pyrolyzed material) The XPS analysis showed that the atomic composition of the catalysts (Table S1) is mainly based on carbon and oxygen, while nitrogen and iron are present in a small percentage (1.90% and 0.12%, respectively). Concerning nitrogen speciation, the relative percentage of pyridinic is the highest of all types of nitrogen atoms and nitrogen coordinated to iron is also present (Figure S1). It was shown before that pyridinic nitrogen and Fe-Nx species have a crucial importance for ORR, behaving as active sites [55].

2.1. Electrochemical Characterization

2.1.1. Catalytic Activity towards ORR

Figure 2 shows the disk current (Figure 2a) and the hydrogen peroxide intermediate percentage (Figure 2b) obtained from the LSV-RRDE experiments, for the Fe-N-C catalyst and bare carbon support. As observed in Figure 2a, Fe-N-C sample is more active toward ORR than the carbon support, in terms of onset potential (E_{onset}), half-wave potential ($E_{1/2}$), and limiting current density (J_{lim}). Those value are similar and even higher as compared to previous reports on other M-N-C materials [5,8,56]. The number of electrons exchanged for the Fe-N-C catalyst approaches to 4 (3.99 ± 0.01 at $E_{1/2}$ V), mainly indicating a direct $4e^-$ transfer mechanism, with a low peroxide percentage (Table S2). This value became slightly lower at higher overpotentials (3.8 ± 0.01 at 0.5 V), for the active role of black pearls in promoting oxygen reduction via a $2e^-$ steps [57].

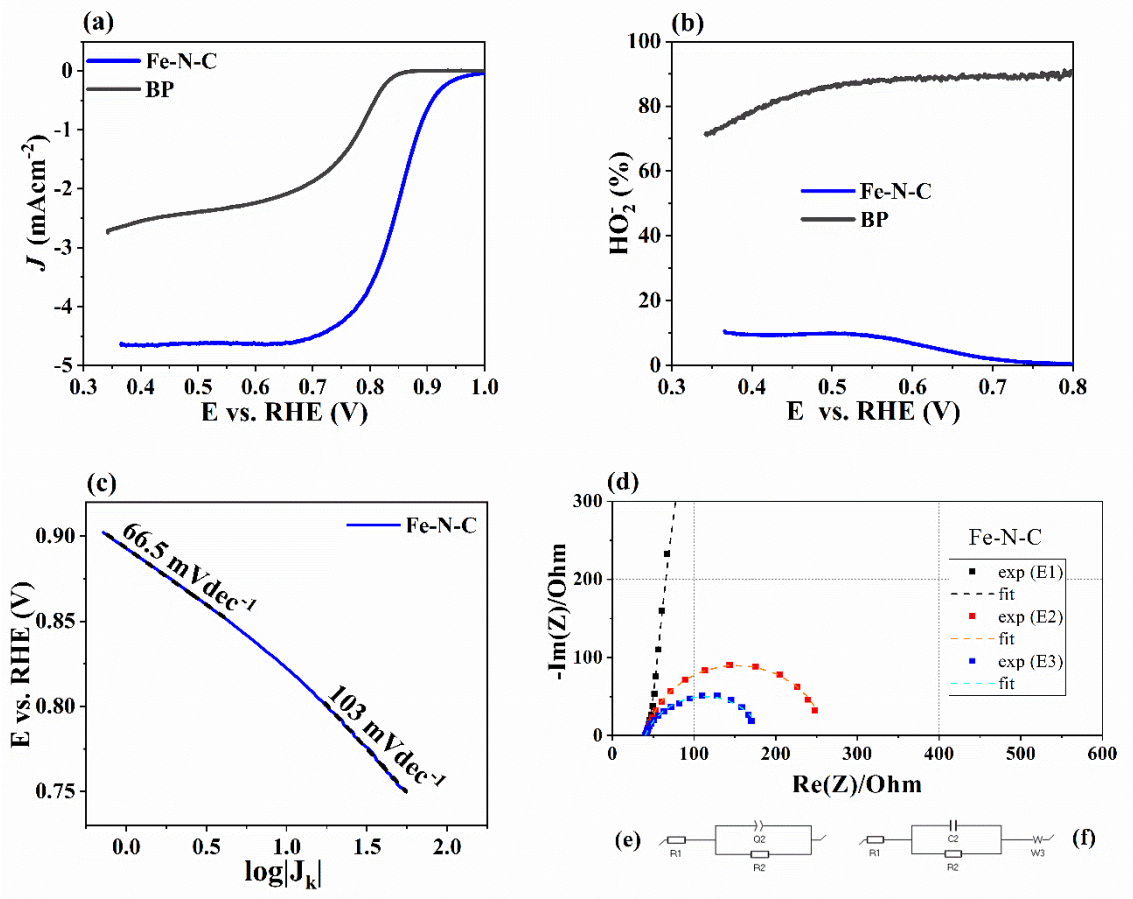

Figure 2. Analysis of ORR activity of Fe-N-C: (a) LSV-RRDE in O_2-saturated 0.1 M KOH; (**b**) HO_2^- percentage; (**c**) Tafel plot; (**d**) Nyquist plots at 0.95 V(E1), 0.85 V (E2), 0.7 V (E3); (**e**,**f**) EIS equivalent circuits.

Figure 2c shows Tafel plot for the Fe-N-C sample, and Table S3 shows the results of Tafel analysis: Tafel slope (2.303RT/αcF), exchange current density (J_0), the cathodic transfer coefficient (αc), according to Equation (1) [58–60]. Fe-N-C shows a low current density (*lcd)* and a high current density (*hcd)* Tafel slope of 55.6 and 103 mVdec^{-1}, respectively, similar to previous reports dealing with Pt-based electrodes in alkaline medium [60,61]. J_0 of 1.2 × 10^{-3} mAcm^{-2} was also comparable to Pt-based electrodes [61,62] and even higher than other M-N-C catalysts reported in literature [63]. As far as ORR mechanism is concerned, the rate determining step (*rds*) of ORR is the second electron transfer and cleavage of the molecular oxygen bond, in agreement with previous reports on ORR on Fe-Nx-C active sites [62,64].

Electrochemical impedance spectroscopy was carried out to obtain further insights on the ORR catalytic activity of Fe-N-C electrode surface. The Nyquist plots (Figure 2d) taken at E1 (onset potential) consist of a tail in the low frequency range; polarizing the electrode at a lower potential value (E2 and E3), the Nyquist plot shows a well-defined semicircle which can be modeled to a Randles-type circuit (Figure 2e). In the equivalent circuit (EC), R1 represents ohmic resistance, R2 represents charge transfer resistance, and Q2 represents a constant phase element related to double layer capacitance (Q2). According to this EC, charge transfer limits the reaction kinetics [65–67], while mass diffusion is limited to a finite and narrow layer. A short Warburg diffusion element (W) was added to model the low-frequency process related to diffusion phenomena.

The fitting provided the following results: R1 was around 40 Ω and represents the resistance of the electrolyte solution (0.1 M KOH). Such a value agrees with resistance values obtained by different authors in previously published works dealing with ORR in 0.1 M KOH [68,69]. Moreover, a value of 31.7 $\Omega^{-1/2}$ was obtained for the Warburg

element. The Q2 value was 2.10 $mFs^{(a-1)}$ (a = 0.875 ± 0.035) at E1 and increased up to 35% as the potential decreased (E2 and E3). Charge transfer resistance (R2) was high at onset potential (2677 ± 79 Ω), while it decreased as the potential decreased and ORR took places (280 ± 3 Ω and 181 ± 2 Ω at E2 and E3, respectively). Since charge transfer resistance across the reaction is strongly correlated with the electrochemical performance, EIS analysis confirmed the ORR activity of the Fe-N-C sample previously discussed by LSV measurements for the Fe-N-C sample.

Durability of the Fe-N-C catalyst was investigated in terms of a start-stop test, by acquiring 7000 CV cycles in N_2-saturated 0.1 M KOH electrolyte (Figure S2). Figure 3a shows ECSA retention over the CV cycles, indicating a good stability in term of ECSA. Hence, Fe-N-C had a higher durability as compared to the state-of-the-art Pt/C electrode, since previous works indicate that it shows a 60 to 80 % ECSA loss over cycling [62,70].

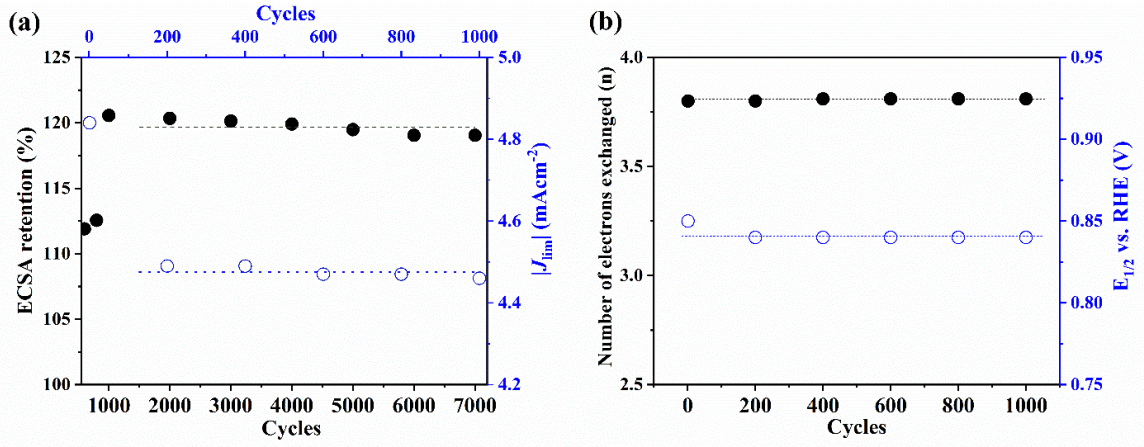

Figure 3. Durability tests of Fe-N-C catalyst: (**a**) ECSA retention (black circles) and J_{lim} values over 7000 cycles (empty blue circles); (**b**) number of electrons exchanged (black circles) and $E_{1/2}$ over 1000 cycles (empty blue circles).

ORR activity over 1000 CV cycles in O_2-saturated electrolyte was also investigated, in terms of variation of E_{onset}, $E_{1/2}$, J_{lim}, n, and HO_2^- percentage (Table S2 and Figure 3). As shown in Figure 3b, n and $E_{1/2}$ were stable over cycling, with a slightly decrease in J_{lim} (Figure 3a). Methanol and SCN^- tolerance were investigated by LSV in O_2-saturated electrolyte (Figure S3). The obtained data showed that ORR activity was not affected by methanol poisoning: in fact, onset potential, half-wave potentials, and limiting current density remained almost constant up to 2 M concentration of methanol in the electrolyte solution (Figure S3a). This finding is in good agreement with previous works reporting MeOH tolerance studies of Fe-N-C catalysts as compared to Pt/C, which shows a considerable decrease in ORR performance above 0.01 M MeOH concentration [71]. Moreover, SCN^- tolerance tests (Figure S3b) indicate a slight decrease in Eonset, (2.1%) E1/2, (3.4%) and J_{lim} (10.2%) parameters. This finding indicates that, although SCN^- is able to bind to the iron center of active sites [40], this effect is moderate in alkaline environments, since OH^- acts as an active site blocker [72,73].

2.1.2. Catalytic Activity towards HER

The activity towards HER for the synthesized Fe-N-C material was also evaluated and compared with Pt/C as state-of-the art catalyst. Figure 4 shows the electrochemical measurements performed in N_2-saturated 0.1 M KOH electrolyte. The HER parameters extrapolated from the LSV curves (Figure 4a) showed a good catalytic activity for the Fe-N-C sample in terms of E_{onset} (350 mV) values and the potential for achieving J = −10 $mAcm^{-2}$ (η_{10}), which is of 478 mV. These values were comparable to those observed for others PGM-Free catalysts (Table 2) [74–76]. As expected, the Pt/C electrode showed lower values of E_{onset} (11 mV) and η_{10} (76 mV). The higher kinetic limitation of the Fe-N-C material is a

consequence of the difference in active sites density between Fe-N-C and Pt/C: M-N-C materials suffer indeed from disadvantages in comparison to metal bulk catalysts due to distance between active sites [77].

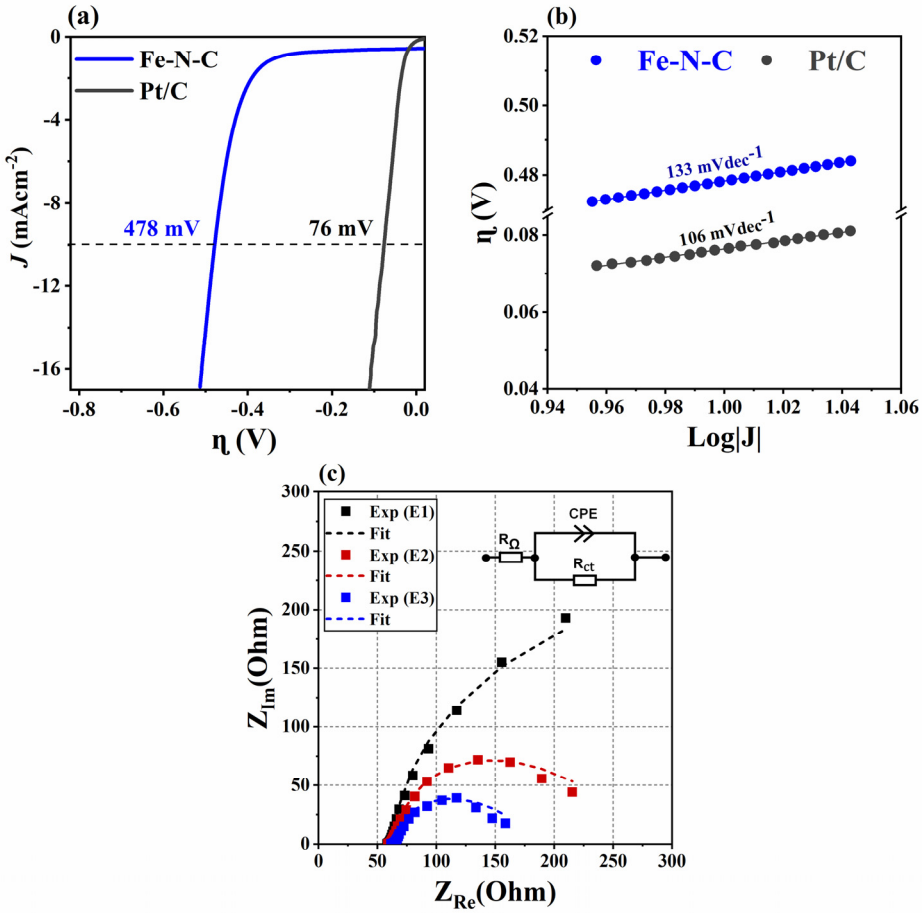

Figure 4. Electrochemical characterization for the Fe-N-C and Pt/C catalysts in N_2-saturated 0.1 M KOH electrolyte: (**a**) LSV curves at 5 mVs^{-1}; (**b**) Tafel plot, and (**c**) Nyquist plot at different potential values and equivalent circuit (inset of Figure 4c) for data fitting (experimental data-pointed line, data fit-dashed line).

Furthermore, the reaction mechanism was investigated from the Tafel plot analysis (Figure 4b). As previously discussed, HER mechanism in alkaline media proceeds through H_2O dissociation: OH^- is released in solution with adsorbed atomic hydrogen bound at the metal surface (Volmer step), then an electrochemical desorption (Heyrovsky step) or Metal-H_{ad} recombination (Tafel step) takes place. However, the Volmer–Heyrovsky reaction preferentially occurs on both metal bulk and single sites M-N-C catalysts at pH > 7 [78–80]. A Tafel slope of 133 and 106 $mVdec^{-1}$ was obtained for Fe-N-C and Pt/C, respectively. These values were in between the predicted Tafel slopes for the combination of the rate-determining Volmer (118 $mVdec^{-1}$) and Heyrovsky (40 $mVdec^{-1}$) steps, suggesting that HER on both electrode surfaces occurs through the Volmer–Heyrovsky reactions described by Equations (1) and (2) in Table S4. An exchange current density (J_0) of 1.30×10^{-3} and 0.44 $mAcm^{-2}$ was achieved in the case of Fe-N-C and Pt/C electrodes, respectively, in good agreement with LSV analysis and reported values in literature [68,76,81–83].

Electrochemical behavior for the HER was also investigated by EIS analysis acquiring Nyquist plots (Figure 4c) at three different potentials: at 0.40 V (E1), 0.45 V (E2-between E_{onset} and η_{10}) and 0.50 V (E3-η_{10}). To model the HER process at the electrode surface, a Randles-type equivalent circuit was adopted, replacing capacitance in the circuit model illustrated in Figure 2e by a constant phase element (inset of Figure 4c). The EIS data fitting

are also reported in Table S5. Nyquist plot analysis showed that solution resistance (R1) was kept around 63 Ohm independent on electrode polarization. Additionally, Q2 changes were negligible, ranging between 3.8 × 10^{-3} and 3.4 × 10^{-3} $S.s^n$ in the investigated potentials, while the observed semicircle related to charge transfer resistance (R2) decreases as the overpotential increases from E_{onset} to η_{10}.

Table 2. HER parameters at a current density of −10 $mAcm^{-2}$ for the synthesized Fe-N-C material and other PGM and PGM-Free catalysts reported in literature.

Catalysts	E_{onset} (mV)	η_{10} (mV)	Tafel Slope ($mVdec^{-1}$)	Ref.
Fe-N-C	350	478	100	this work
Fe^{2+}Ni@NCF	-	484	148	[80]
Fe^{2+}Ni-PBA	-	526	213	[80]
Fe/Fe_3C@N-C-2	-	560	113	[76]
0.3 Ni-Fe-Pt NCs	476	490	89	[75]
Fe_2O_3/NS-C-800	110	270	165	[84]
$Fe_2O_{3(1)}$-$Co_{(1)}$ NPs-N-GR	178	410	77	[74]
Ni_3S_2/MWCNT-NC	-	480	102	[85]
MoS_2–ZnO	-	490	171	[86]
Pt/C	11	76	106	this work
Pt/C	30	101	64	[80]

Concerning the performance as a bifunctional Fe-N-C catalyst, the electrochemical analysis showed a higher ORR activity as compared to HER as expected. This behavior can be related to the distance between the Fe-N-C active sites, more critical for H_2 evolution than for oxygen reduction. Although the iron content used to synthesize the Fe-based catalyst have been adopted to avoid formation of inactive metal-based species, the used percentage of iron is still under a saturation range, since iron oxide or metallic particles phases were not evidenced as suggested from XRD analysis, also in agreement with previous studies reported in literature [87,88]. HER activity of our Fe-N-C electrocatalyst is lower as compared to activity of different M-N-C catalysts synthesized with a higher metal concentration [37,74]; therefore, an enhancement in HER activity could be achieved by tailoring iron content to obtain higher density of Fe-based active sites [89].

3. Materials and Methods

3.1. Materials

Carbon Black pearls 2000 (BP) and Imidazole (>98.0%) were supplied by Cabot corporation (Billerica, MA, US) and TCI Europe N.V (Zwijndrecht Belgium), respectively. $Fe(C_2H_3O_2)_2$, HNO_3, *N*,*N*-Dimethylformamide, and Nafion solution were supplied from Sigma-Aldrich (St. Louis, MO, US). Methanol and potassium thiocyanate–KSCN were supplied by Merk. Pt/C (40% platinum on carbon black was purchased by Alfa Aesar (Karlsruhe; Germany). Millipore water (Merk, 18.2 MΩcm) was used in all the experiments.

Carbon Support and Catalyst Preparation

The Fe-N-C electrocatalyst was prepared as previously described [69]. Briefly, 400 mg of BP (previously activated in refluxing concentrated HNO_3 solution) were added in an water/acetone solution (V = 160 mL, 10 wt. % of acetone), followed by the addition of imidazole (400 mg) under stirring at room temperature. Iron acetate was then added to an iron content of 0.2 wt.%. The suspension was stirred at room temperature for 2 h, followed by solvent removal by evaporation at 70 °C overnight. The Fe-N-C precursor was grounded and pyrolyzed in anhydrous NH_3 flow in two steps: a first heat treatment at

400 °C (20 °Cmin^{-1} for 1 h) and a second one at 800 °C (25 °Cmin^{-1} for 1 h) to obtain the Fe-N-C catalyst.

3.2. Methods

Thermogravimetric analysis (TGA) of the catalyst precursors was performed by using a TGA/DSC1 Star System (Mettler Toledo, Columbus, Ohio, US): heating rate of 5 °C min^{-1} under a N_2 flow. Powder X-ray diffraction (XRD) patterns were acquired by a Philips PW1730 diffractometer with Cu K αradiation (λ = 1.5406 Å), and a Leo Supra 35 field-emission scanning electron microscope (Carl Zeiss, Oberkochen, Germany) was used for the investigation of samples' morphology. Raman spectroscopy was carried out by using a DXR Raman Microscope (Thermo Scientific, Waltham, MA, USA): laser excitation wavelength 532 nm with a 10× objective, laser power 0.1 mW.

3.2.1. Electrochemical Characterization

A three-electrode electrochemical cell was used for the electrochemical experiments: the working electrode (WE) was either a rotating ring disk electrode (RRDE-AFE6R2GCPT, Disk OD = 5.5 mm; Ring OD = 8.50 mm; Ring ID = 6.50 mm) or a glassy carbon disk (AFE1XFP030GCR, 3 mm disk diameter, 0.071 cm^2, for ORR and HER experiments, respectively, both purchased by Pine Research Instrumentation (Durham, NC, US). A graphite rod was used as counter electrode and a saturated calomel electrode (SCE, Amel 303/SCG/12) was used as reference electrode. A VMP3 Potentiostat (Bio Logic Science Instruments, Seyssinet-Pariset, France) equipped with an EC-Lab V10.18 software was used for the electrochemical measurements. The potential values for all electrochemical tests were converted to the reversible hydrogen electrode (RHE).

The WE for the ORR experiments was modified with the catalyst ink as previously reported [62] to a catalyst loading of 0.23 mgcm^{-2} and 0.5 mgcm^{-2} for ORR and HER experiments, respectively. A WE based on Pt/C was also prepared as control, by dispersing 1 mg of Pt/C 40 wt.% in 1 mL of DI, 0.3 mL isopropanol, and 5 µL Nafion solution 5 wt.%. The dispersion was treated in an ultrasonic bath for 30 min at 10 °C, and the ink dropped (4.2 µL) onto GC (0.0455 mgcm^{-2} catalyst loading corresponding to 0.0182 mgcm^{-2} Pt loading, as generally reported in literature [90]).

3.2.2. Cyclic Voltammetry (CV)

CV was carried out in either N_2 or O_2—saturated aqueous KOH 0.1 M; prior measurements, the electrode was activated by performing 100 to 300 CV cycles at 500 and 5 mVs^{-1}. ECSA was obtained from CV in N_2-saturated KOH by integrating capacitive current over a potential window of 0.90 V vs. RHE, assuming a specific capacitance of 0.2 Fm^{-2} [62].

LSV-RRDE experiments for assessing ORR activity were carried out at a scan rate of 5 mVs^{-1} and electrode rotation speed of 1600 rpm, with the Pt ring polarized at 1.2 V vs. RHE [91]. Current density reported in the Figures within the manuscript was background corrected and the potentials were iR-compensated. The number of electrons transferred (n) and HO_2^- produced were calculated as previously reported [62]. Methanol tolerance was investigated by LSV in O_2-saturated electrolyte, before and after addition of increasing aliquots of methanol to the electrolyte solution to achieve the following concentrations: 0.01, 0.05, 0.1, 1, and 2 M. LSV curves were acquired at a scan rate of 5 mVs^{-1} and a rotation speed of 1600 rpm with a poisoning time of 5 min after the alcohol addiction [71]. The SCN^- poisoning test was also performed by acquiring LSV curves before and after addition of KSCN (0.01 M) with a poisoning time of 40 min [79].

LSV-RRDE experiments for assessing HER activity were carried out in N_2-saturated electrolyte at a scan rate of 5 mVs^{-1} from 0.11 to −0.59 V vs. RHE. The reported potential values were *i*R-compensated at 100% by using the impedance spectroscopy. E_{onset} and the overpotential necessary to achieve a 10 mA cm^{-2} current density (η_{10}) were extrapolated from the LSV curves.

Tafel plots was obtained by plotting E (electrode potential) vs the logarithm of J_k (kinetic current density) according to the Equation (1):

$$E = E^0 + \frac{2.303RT}{\alpha_c F} \log J_0 - \frac{2.303RT}{\alpha_c F} \log J_k \quad (1)$$

where E^0 is standard potential, R is the universal gas constant, T is temperature, F is the Faraday constant, α_c is the transfer coefficient, J_0 is the exchange current density, and J_k was calculated with the Equation (2), where J_D is the limiting current density:

$$J_k(E) = \left| \frac{J_D \, J(E)}{J_D - J(E)} \right| \quad (2)$$

Electrochemical Impedance Spectroscopy (EIS) spectra was carried out under hydrodynamic conditions at 1600 rpm and at different potential values E1 (E_{onset} = 0.95 V), E2 ($E_{1/2}$ = 0.85 V), E3 (E@J_{lim} = 0.7 V) in a 50 mHz–100 kHz frequency range with an applied alternating voltage with an amplitude of 10 mV, for ORR experiments. As far as HER experiments are concerned, EIS analysis was performed under static conditions at the potential values of 0.39, 0.44 and 0.49 V vs. RHE. EIS spectra were modeled by means of the EC-Lab ZFit impedance fitting tools.

The durability of Fe-N-C was evaluated by 7000 CV cycles (500 mVs^{-1} in N_2-saturated electrolyte) to evaluate the ECSA changes, according to a well-established protocol [92]. tests were carried out according to well established protocols [92]. In addition, CV was carried out to study possible changes in catalytic activity over CV cycles (scan rate of 500 mVs^{-1} in oxygen-saturated electrolyte).

4. Conclusions

An iron–nitrogen–carbon catalyst was developed by impregnating carbon black pearls with iron acetate and imidazole as a nitrogen source, followed by pyrolysis steps in ammonia atmosphere. XRD analysis does not indicates presence of metallic or metal oxide phases, suggesting that the nitrogen-containing precursor and pyrolysis in ammonia atmosphere were an effective combination to functionalize the carbon matrix, avoiding iron precipitation as impurities or less catalytic active sites, in agreement with the Raman and XPS analysis that showed a high I_G/I_D ratio and a high content of active catalytic sites such as pyridinic and Fe-N_x-C moieties. In addition, pyrolysis in ammonia also preserves the carbon support morphology leading to a high ECSA. The Fe-N-C catalyst showed a high ORR activity characterized by a direct four electron transfer mechanism, high onset potential (0.95 V), half-wave potential (0.85 V), and limiting current density (-4.63 $mAcm^{-2}$), as pointed out by the electrochemical characterization. A good durability was also indicated by stable values of ECSA and ORR parameters over 7000 and 1000 CV cycles, respectively. The catalysts also displayed a good tolerance to methanol and SCN^-, as indicated by only slight variations of ORR parameters after the addition of the contaminants.

Catalytic performance towards HER showed an onset potential of 0.35 V, and a current density of -10 mA cm^{-2} was reached when overpotential achieved a value of 0.48 V. Tafel analysis showed that HER proceeds through Volmer–Heyrovsky reaction and a higher kinetic limitation is observed for the HER, despite ORR as compared to the state-of-the art Pt-based catalyst. Difference in activity towards both reactions can be related to the effect of density and proximity of the active sites, which is more critical for the HER since combination of hydrogen atoms demands short distances between the metal-based sites. Despite the promising results obtained, a higher HER activity could be achieved by tailoring the iron content in order to increase the density of the active sites. The body of the electrochemical analysis indicated that Fe-N-C can be a potential candidate as bifunctional ORR/HER cathodes to replace PGM materials in alkaline fuel cells, microbial fuel cells and microbial electrolysis cells.

Supplementary Materials: The following are available online at https://www.mdpi.com/article/10.3390/catal11121525/s1, Table S1: Atomic percentage of the elements in Fe-N-C catalysts and relative content of the different types of nitrogen, estimated from XPS. Figure S1: N 1 s XPS spectra for the Fe-N-C catalyst. Table S2: Onset potential (E_{onset}), half-wave potential ($E_{1/2}$), limiting current density (J_{lim}), number of electrons transferred (n) and HO_2^- percentage at 0.5 V vs. RHE over CV cycles in O_2-saturated 0.1 M KOH.; Table S3: Electrochemical parameters extrapolated from the Tafel analysis, Figure S2: Cyclic voltammograms in N_2-saturated electrolyte at a scan rate of 5 mVs^{-1} over 7000 cycles for the Fe-N-C sample; Figure S3: LSV curves for the Fe-N-C catalyst in O_2-saturated KOH 0.1 M electrolyte at a scan rate of 5 mVs^{-1} and 1600 rpm before and after the addition of 0.01–2.00 M methanol (a) and 0.01 M KSCN in the electrolyte. Table S4: HER mechanism in alkaline environment; Table S5: HER electrochemical parameters obtained from EIS data fitting.

Author Contributions: Conceptualization, A.D. and B.M.; Data curation, W.d.S.F. and B.M.; Funding acquisition, A.D.; Investigation, W.d.S.F., P.P.M.P., A.D. and B.M.; Methodology, W.d.S.F. and B.M.; Project administration, B.M.; Resources, A.D. and B.M.; Supervision, A.D. and B.M.; Writing—original draft, W.d.S.F. and P.P.M.P.; Writing—review & editing, W.d.S.F. and B.M. All authors have read and agreed to the published version of the manuscript.

Funding: This research was funded by Regione Lazio through the project POR FESR LAZIO 2014–2020, No A0375-2020-36492.

Data Availability Statement: The data used to support the findings of this study are available within the article and its supplementary materials.

Acknowledgments: The authors acknowledge Cadia D'Ottavi (Department Chemical Science and Technologies of the University of Rome Tor Vergata) for her valuable technical support.

Conflicts of Interest: The authors declare no conflict of interest.

References

1. Mecheri, B.; Gokhale, R.R.; Santoro, C.; De Oliveira, M.A.C.; D'Epifanio, A.; Licoccia, S.; Serov, A.; Artyushkova, K.; Atanassov, P. Oxygen Reduction Reaction Electrocatalysts Derived from Iron Salt and Benzimidazole and Aminobenzimidazole Precursors and Their Application in Microbial Fuel Cell Cathodes. *ACS Appl. Energy Mater.* **2018**, *1*, 5755–5765. [CrossRef]
2. De Oliveira, M.A.C.; Mecheri, B.; D'Epifanio, A.; Zurlo, F.; Licoccia, S. Optimization of PGM-free cathodes for oxygen reduction in microbial fuel cells. *Electrochim. Acta* **2020**, *334*, 135650. [CrossRef]
3. Santoro, C.; Gokhale, R.; Mecheri, B.; D'Epifanio, A.; Licoccia, S.; Serov, A.; Artyushkova, K.; Atanassov, P. Design of Iron(II) Phthalocyanine-Derived Oxygen Reduction Electrocatalysts for High-Power-Density Microbial Fuel Cells. *ChemSusChem* **2017**, *10*, 3243–3251. [CrossRef]
4. Seh, Z.W.; Kibsgaard, J.; Dickens, C.F.; Chorkendorff, I.; Nørskov, J.K.; Jaramillo, T.F. Combining theory and experiment in electrocatalysis: Insights into materials design. *Science* **2017**, *355*, eaad4998. [CrossRef]
5. Jia, H.-L.; Zhao, J.; Gu, L.; Peng, Z.-J.; Bao, Z.-L.; Sun, X.-L.; Guan, M.-Y. Highly active Co–N-doped graphene as an efficient bifunctional electrocatalyst (ORR/HER) for flexible all-solid-state zinc–air batteries. *Sustain. Energy Fuels* **2020**, *4*, 6165–6173. [CrossRef]
6. Ding, J.; Ji, S.; Wang, H.; Pollet, B.G.; Wang, R. Mesoporous CoS/N-doped Carbon as HER and ORR Bifunctional Electrocatalyst for Water Electrolyzers and Zinc-Air Batteries. *ChemCatChem* **2018**, *11*, 1026–1032. [CrossRef]
7. Wang, J.; Xu, F.; Jin, H.; Chen, Y.; Wang, Y. Non-Noble Metal-based Carbon Composites in Hydrogen Evolution Reaction: Fundamentals to Applications. *Adv. Mater.* **2017**, *29*. [CrossRef]
8. Sgarbi, R.; Kumar, K.; Jaouen, F.; Zitolo, A.; Ticianelli, E.A.; Maillard, F. Oxygen reduction reaction mechanism and kinetics on M-NxCy and M@N-C active sites present in model M-N-C catalysts under alkaline and acidic conditions. *J. Solid State Electrochem.* **2019**, *25*, 45–56. [CrossRef]
9. Yan, X.; Li, X.; Fu, C.; Lin, C.; Hu, H.; Shen, S.; Wei, G.; Zhang, J. Large specific surface area S-doped Fe–N–C electrocatalysts derived from Metal–Organic frameworks for oxygen reduction reaction. *Prog. Nat. Sci.* **2020**, *30*, 896–904. [CrossRef]
10. Jin, L.; Zhu, B.; Wang, X.; Zhang, L.; Song, D.; Guo, J.; Tao, H. Facile Synthesis of the Amorphous Carbon Coated Fe-N-C Nanocatalyst with Efficient Activity for Oxygen Reduction Reaction in Acidic and Alkaline Media. *Materials* **2020**, *13*, 4551. [CrossRef]
11. Ketpang, K.; Boonkitkoson, A.; Pitipuech, N.; Poompipatpong, C.; Sanetuntikul, J.; Shanmugam, S. Highly Active and Durable Transition Metal-Coordinated Nitrogen Doped Carbon Electrocatalyst for Oxygen Reduction Reaction in Neutral Media. *E3S Web Conf.* **2020**, *141*, 1005. [CrossRef]
12. Wang, D.; Hu, J.; Yang, J.; Xiao, K.; Liang, S.; Xu, J.; Liu, B.; Hou, H. Fe and N co-doped carbon derived from melamine resin capsuled biomass as efficient oxygen reduction catalyst for air-cathode microbial fuel cells. *Int. J. Hydrogen Energy* **2019**, *45*, 3163–3175. [CrossRef]

13. Chen, Y.; Zheng, Y.; Yue, X.; Huang, S. Hydrogen evolution reaction in full pH range on nickel doped tungsten carbide nanocubes as efficient and durable non-precious metal electrocatalysts. *Int. J. Hydrogen Energy* **2020**, *45*, 8695–8702. [CrossRef]
14. Santoro, C.; Serov, A.; Artyushkova, K.; Atanassov, P. Platinum group metal-free oxygen reduction electrocatalysts used in neutral electrolytes for bioelectrochemical reactor applications. *Curr. Opin. Electrochem.* **2020**, *23*, 106–113. [CrossRef]
15. Li, Y.; Li, Q.; Wang, H.; Zhang, L.; Wilkinson, D.P.; Zhang, J. Recent Progresses in Oxygen Reduction Reaction Electrocatalysts for Electrochemical Energy Applications. *Electrochem. Energy Rev.* **2019**, *2*, 518–538. [CrossRef]
16. Choi, C.H.; Kwon, H.C.; Yook, S.; Shin, H.; Kim, H.; Choi, M. Hydrogen Peroxide Synthesis via Enhanced Two-Electron Oxygen Reduction Pathway on Carbon-Coated Pt Surface. *J. Phys. Chem. C* **2014**, *118*, 30063–30070. [CrossRef]
17. Alsudairi, A.; Li, J.; Ramaswamy, N.; Mukerjee, S.; Abraham, K.M.; Jia, Q. Resolving the Iron Phthalocyanine Redox Transitions for ORR Catalysis in Aqueous Media. *J. Phys. Chem. Lett.* **2017**, *8*, 2881–2886. [CrossRef]
18. Harnisch, F.; Savastenko, N.A.; Zhao, F.; Steffen, H.; Brüser, V.; Schröder, U. Comparative study on the performance of pyrolyzed and plasma-treated iron(II) phthalocyanine-based catalysts for oxygen reduction in pH neutral electrolyte solutions. *J. Power Sources* **2009**, *193*, 86–92. [CrossRef]
19. Iannaci, A.; Mecheri, B.; D'Epifanio, A.; Elorri, M.J.L.; Licoccia, S. Iron–nitrogen-functionalized carbon as efficient oxygen reduction reaction electrocatalyst in microbial fuel cells. *Int. J. Hydrogen Energy* **2016**, *41*, 19637–19644. [CrossRef]
20. Nguyen, M.-T.; Mecheri, B.; Iannaci, A.; D'Epifanio, A.; Licoccia, S. Iron/Polyindole-based Electrocatalysts to Enhance Oxygen Reduction in Microbial Fuel Cells. *Electrochim. Acta* **2016**, *190*, 388–395. [CrossRef]
21. De Oliveira, M.A.C.; Mecheri, B.; D'Epifanio, A.; Placidi, E.; Arciprete, F.; Valentini, F.; Perandini, A.; Valentini, V.; Licoccia, S. Graphene oxide nanoplatforms to enhance catalytic performance of iron phthalocyanine for oxygen reduction reaction in bioelectrochemical systems. *J. Power Sources* **2017**, *356*, 381–388. [CrossRef]
22. Ramaswamy, N.; Mukerjee, S. Fundamental Mechanistic Understanding of Electrocatalysis of Oxygen Reduction on Pt and Non-Pt Surfaces: Acid versus Alkaline Media. *Adv. Phys. Chem.* **2012**, *2012*, 1–17. [CrossRef]
23. Osmieri, L. Transition Metal–Nitrogen–Carbon (M–N–C) Catalysts for Oxygen Reduction Reaction. Insights on Synthesis and Performance in Polymer Electrolyte Fuel Cells. *ChemEngineering* **2019**, *3*, 16. [CrossRef]
24. Gong, M.; Wang, D.-Y.; Chen, C.-C.; Hwang, B.-J.; Dai, H. A mini review on nickel-based electrocatalysts for alkaline hydrogen evolution reaction. *Nano Res.* **2015**, *9*, 28–46. [CrossRef]
25. Mahmood, N.; Yao, Y.; Zhang, J.-W.; Pan, L.; Zhang, X.; Zou, J.-J. Electrocatalysts for Hydrogen Evolution in Alkaline Electrolytes: Mechanisms, Challenges, and Prospective Solutions. *Adv. Sci.* **2017**, *5*, 1700464. [CrossRef]
26. Wei, J.; Zhou, M.; Long, A.; Xue, Y.; Liao, H.; Wei, C.; Xu, Z.J. Heterostructured Electrocatalysts for Hydrogen Evolution Reaction Under Alkaline Conditions. *Nano-Micro Lett.* **2018**, *10*, 1–15. [CrossRef]
27. Benck, J.D.; Hellstern, T.R.; Kibsgaard, J.; Chakthranont, P.; Jaramillo, T.F. Catalyzing the Hydrogen Evolution Reaction (HER) with Molybdenum Sulfide Nanomaterials. *ACS Catal.* **2014**, *4*, 3957–3971. [CrossRef]
28. Fan, X.; Kong, F.; Kong, A.; Chen, A.; Zhou, Z.; Shan, Y. Covalent Porphyrin Framework-Derived Fe2P@Fe4N-Coupled Nanoparticles Embedded in N-Doped Carbons as Efficient Trifunctional Electrocatalysts. *ACS Appl. Mater. Interfaces* **2017**, *9*, 32840–32850. [CrossRef] [PubMed]
29. Hoang, V.C.; Gomes, V.G.; Dinh, K.N. Ni- and P-doped carbon from waste biomass: A sustainable multifunctional electrode for oxygen reduction, oxygen evolution and hydrogen evolution reactions. *Electrochim. Acta* **2019**, *314*, 49–60. [CrossRef]
30. Ying, L.; Sun, S.; Liu, W.; Zhu, H.; Zhu, Z.; Liu, A.; Yang, L.; Lu, S.; Duan, F.; Yang, C.; et al. Heterointerface engineering in bimetal alloy/metal carbide for superior hydrogen evolution reaction. *Renew. Energy* **2020**, *161*, 1036–1045. [CrossRef]
31. Kamali, S.; Zhiani, M.; Tavakol, H. Synergism effect of first row transition metals in experimental and theoretical activity of NiM/rGO alloys at hydrogen evolution reaction in alkaline electrolyzer. *Renew. Energy* **2020**, *154*, 1122–1131. [CrossRef]
32. Zhao, X.; Yin, F.; He, X.; Chen, B.; Li, G. Enhancing hydrogen evolution reaction activity on cobalt oxide in alkaline electrolyte by doping inactive rare-earth metal. *Electrochim. Acta* **2020**, *363*, 137230. [CrossRef]
33. Zhang, K.; Liu, J.; Xiao, W.; Yan, C. Electrodeposition of graded Ni-S film for hydrogen evolution reaction. *Mater. Lett.* **2017**, *193*, 77–80. [CrossRef]
34. Wang, H.; Lu, Z.; Kong, D.; Sun, J.; Hymel, T.M.; Cui, Y. Electrochemical Tuning of MoS 2 Nanoparticles on Three-Dimensional Substrate for Efficient Hydrogen. *ACS Nano* **2014**, *8*, 4940–4947. [CrossRef]
35. Paul, S.C.; Dey, S.C.; Molla, A.I.; Islam, S.; Debnath, S.; Miah, M.Y.; Ashaduzzaman, M.; Sarker, M. Nanomaterials as electrocatalyst for hydrogen and oxygen evolution reaction: Exploitation of challenges and current progressions. *Polyhedron* **2020**, *193*, 114871. [CrossRef]
36. Yuan, Q.; Yu, Y.; Sherrell, P.C.; Chen, J.; Bi, X. Fe/Co-based Bimetallic MOF-derived Co 3 Fe 7 @NCNTFs Bifunctional Electrocatalyst for High-Efficiency Overall Water Splitting. *Chem. Asian J.* **2020**, *15*, 1728–1735. [CrossRef]
37. Fang, W.; Wang, J.; Hu, Y.; Cui, X.; Zhu, R.; Zhang, Y.; Yue, C.; Dang, J.; Cui, W.; Zhao, H.; et al. Metal-organic framework derived Fe-Co-CN/reduced graphene oxide for efficient HER and OER. *Electrochim. Acta* **2020**, *365*, 137384. [CrossRef]
38. Jin, H.; Wang, J.; Su, D.; Wei, Z.; Pang, Z.; Wang, Y. In situ Cobalt–Cobalt Oxide/N-Doped Carbon Hybrids as Superior Bifunctional Electrocatalysts for Hydrogen and Oxygen Evolution. *J. Am. Chem. Soc.* **2015**, *137*, 2688–2694. [CrossRef] [PubMed]
39. Pi, C.; Huang, C.; Yanga, Y.; Songa, H.; Zhanga, X.; Zheng, Y.; Gaoab, B.; Fua, J.; Chu, P.K.; Huoa, K. In situ formation of N-doped carbon-coated porous MoP nanowires: A highly efficient electrocatalyst for hydrogen evolution reaction in a wide pH range. *Appl. Catal. B Environ.* **2019**, *263*, 118358. [CrossRef]

40. Wang, Q.; Zhou, Z.-Y.; Lai, Y.-J.; You, Y.; Liu, J.-G.; Wu, X.-L.; Terefe, E.; Chen, C.; Song, L.; Rauf, M.; et al. Phenylenediamine-Based FeNx/C Catalyst with High Activity for Oxygen Reduction in Acid Medium and Its Active-Site Probing. *J. Am. Chem. Soc.* **2014**, *136*, 10882–10885. [CrossRef]
41. Chen, Z.; Higgins, D.; Yu, A.; Zhang, L.; Zhang, J. A review on non-precious metal electrocatalysts for PEM fuel cells. *Energy Environ. Sci.* **2011**, *4*, 3167–3192. [CrossRef]
42. Li, J.; Jaouen, F. Structure and activity of metal-centered coordination sites in pyrolyzed metal-nitrogen-carbon catalysts for the electrochemical reduction of O_2. *Curr. Opin. Electrochem.* **2018**, *9*, 198–206. [CrossRef]
43. Patel, A. Functionalization of Keggin-type nickel substituted phosphotungstate by imidazole: Synthesis, characterization, and catalytic activity. *J. Mater. Sci.* **2016**, *52*, 4689–4699. [CrossRef]
44. Ramirez, J.H.; Costa, C.; Madeira, L.M.; Mata, G.; Vicente, M.A.; Cervantes, M.L.R.; Lopez-Peinado, A.J.; Martin-Aranda, R.M. Fenton-like oxidation of Orange II solutions using heterogeneous catalysts based on saponite clay. *Appl. Catal. B Environ.* **2007**, *71*, 44–56. [CrossRef]
45. Jawhari, T.; Roid, A.; Casado, J. Raman spectroscopic characterization of some commercially available carbon black materials. *Carbon* **1995**, *33*, 1561–1565. [CrossRef]
46. Ferrari, A.C. Raman spectroscopy of graphene and graphite: Disorder, electron–phonon coupling, doping and nonadiabatic effects. *Solid State Commun.* **2007**, *143*, 47–57. [CrossRef]
47. Han, J.; Bao, H.; Wang, J.-Q.; Zheng, L.; Sun, S.; Wang, Z.L.; Sun, C. 3D N-doped ordered mesoporous carbon supported single-atom Fe-N-C catalysts with superior performance for oxygen reduction reaction and zinc-air battery. *Appl. Catal. B Environ.* **2020**, *280*, 119411. [CrossRef]
48. Yin, P.; Wang, W.; Rao, H.; Wang, G.; Sun, M.; Jiang, Y.; Wang, Y.; Zou, P.; Wang, X.; Zhao, Q.; et al. One-step prepared prussian blue/porous carbon composite derives highly efficient Fe–N–C catalyst for oxygen reduction. *Int. J. Hydrogen Energy* **2020**, *45*, 15100–15111. [CrossRef]
49. Tuo, J.; Lin, Y.; Zhu, Y.; Jiang, H.; Li, Y.; Cheng, L.; Pang, R.; Shen, J.; Song, L.; Li, C. Local structure tuning in Fe-N-C catalysts through support effect for boosting CO_2 electroreduction. *Appl. Catal. B Environ.* **2020**, *272*. [CrossRef]
50. Osmieri, L.; Escudero-Cid, R.; Armandi, M.; Videla, A.M.; Fierro, J.L.G.; Ocón, P.; Specchia, S. Fe-N/C catalysts for oxygen reduction reaction supported on different carbonaceous materials. Performance in acidic and alkaline direct alcohol fuel cells. *Appl. Catal. B Environ.* **2017**, *205*, 637–653. [CrossRef]
51. Sadezky, A.; Muckenhuber, H.; Grothe, H.; Niessner, R.; Pöschl, U. Raman microspectroscopy of soot and related carbonaceous materials: Spectral analysis and structural information. *Carbon* **2005**, *43*, 1731–1742. [CrossRef]
52. Vollebregt, S.; Ishihara, R.; Tichelaar, F.; Hou, Y.; Beenakker, C. Influence of the growth temperature on the first and second-order Raman band ratios and widths of carbon nanotubes and fibers. *Carbon* **2012**, *50*, 3542–3554. [CrossRef]
53. Gambou-Bosca, A.; Belanger, D. Chemical Mapping and Electrochemical Performance of Manganese Dioxide/Activated Carbon Based Composite Electrode for Asymmetric Electrochemical Capacitor. *J. Electrochem. Soc.* **2015**, *162*, A5115–A5123. [CrossRef]
54. Meng, H.; Larouche, N.; Lefèvre, M.; Jaouen, F.; Stansfield, B.; Dodelet, J.-P. Iron porphyrin-based cathode catalysts for polymer electrolyte membrane fuel cells: Effect of NH3 and Ar mixtures as pyrolysis gases on catalytic activity and stability. *Electrochim. Acta* **2010**, *55*, 6450–6461. [CrossRef]
55. Artyushkova, K.; Serov, A.; Rojas-Carbonell, S.; Atanassov, P. Chemistry of Multitudinous Active Sites for Oxygen Reduction Reaction in Transition Metal-Nitrogen-Carbon Electrocatalysts. *J. Phys. Chem. C* **2015**, *119*, 25917–25928. [CrossRef]
56. Gokhale, R.; Chen, Y.; Serov, A.; Artyushkova, K.; Atanassov, P. Direct synthesis of platinum group metal-free Fe-N-C catalyst for oxygen reduction reaction in alkaline media. *Electrochem. Commun.* **2016**, *72*, 140–143. [CrossRef]
57. Castegnaro, M.; Paschoalino, W.J.; Fernandes, M.R.; Balke, B.; Alves, M.D.C.; Ticianelli, E.A.; Morais, J. Pd–M/C (M = Pd, Cu, Pt) Electrocatalysts for Oxygen Reduction Reaction in Alkaline Medium: Correlating the Electronic Structure with Activity. *Langmuir* **2017**, *33*, 2734–2743. [CrossRef]
58. Guidelli, R.; Compton, R.G.; Feliu, J.; Gileadi, E.; Lipkowski, J.; Schmickler, W.; Trasatti, S. Defining the transfer coefficient in electrochemistry: An assessment (IUPAC Technical Report). *Pure Appl. Chem.* **2014**, *86*, 245–258. [CrossRef]
59. Guidelli, R.; Compton, R.G.; Feliu, J.; Gileadi, E.; Lipkowski, J.; Schmickler, W.; Trasatti, S. Definition of the transfer coefficient in electrochemistry (IUPAC Recommendations 2014). *Pure Appl. Chem.* **2014**, *86*, 259–262. [CrossRef]
60. Holewinski, A.; Linic, S. Elementary Mechanisms in Electrocatalysis: Revisiting the ORR Tafel Slope. *J. Electrochem. Soc.* **2012**, *159*, H864–H870. [CrossRef]
61. Perez, J.; Gonzalez, E.; Ticianelli, E. Oxygen electrocatalysis on thin porous coating rotating platinum electrodes. *Electrochim. Acta* **1998**, *44*, 1329–1339. [CrossRef]
62. Freitas, W.D.S.; D'Epifanio, A.; Ficca, V.C.; Placidi, E.; Arciprete, F.; Mecheri, B. Tailoring active sites of iron-nitrogen-carbon catalysts for oxygen reduction in alkaline environment: Effect of nitrogen-based organic precursor and pyrolysis atmosphere. *Electrochim. Acta* **2021**, *391*, 138899. [CrossRef]
63. Osmieri, L.; Videla, A.H.A.M.; Specchia, S. The use of different types of reduced graphene oxide in the preparation of Fe-N-C electrocatalysts: Capacitive behavior and oxygen reduction reaction activity in alkaline medium. *J. Solid State Electrochem.* **2016**, *20*, 3507–3523. [CrossRef]
64. Jaouen, F. O2 Reduction Mechanism on Non-Noble Metal Catalysts for PEM Fuel Cells. Part II: A Porous-Electrode Model to Predict the Quantity of H2O2 Detected by Rotating Ring-Disk Electrode. *J. Phys. Chem. C* **2009**, *113*, 15433–15443. [CrossRef]

65. Farahani, F.S.; Mecheri, B.; Majidi, M.R.; de Oliveira, M.A.C.; D'Epifanio, A.; Zurlo, F.; Placidi, E.; Arciprete, F.; Licoccia, S. MnOx-based electrocatalysts for enhanced oxygen reduction in microbial fuel cell air cathodes. *J. Power Sources* **2018**, *390*, 45–53. [CrossRef]
66. Boillot, M.; Didierjean, S.; Lapicque, F. Impedance of a rotating disc electrode with a reversible reaction. *J. Appl. Electrochem.* **2004**, *34*, 1191–1197. [CrossRef]
67. Fu, Y.; Poizeau, S.; Bertei, A.; Qi, C.; Mohanram, A.; Pietras, J.; Bazant, M. Heterogeneous electrocatalysis in porous cathodes of solid oxide fuel cells. *Electrochim. Acta* **2015**, *159*, 71–80. [CrossRef]
68. Sheng, W.; Gasteiger, H.; Shao-Horn, Y. Hydrogen Oxidation and Evolution Reaction Kinetics on Platinum: Acid vs Alkaline Electrolytes. *J. Electrochem. Soc.* **2010**, *157*, B1529. [CrossRef]
69. Roldán, C.A.C.; González-Huerta, R.G.; Alonso-Vante, N. Experimental Protocol for HOR and ORR in Alkaline Electrochemical Measurements. *J. Electrochem. Soc.* **2018**, *165*, J3001–J3007. [CrossRef]
70. Zadick, A.; Dubau, L.; Sergent, N.; Berthomé, G.; Chatenet, M. Huge Instability of Pt/C Catalysts in Alkaline Medium. *ACS Catal.* **2015**, *5*, 4819–4824. [CrossRef]
71. Sebastián, D.; Serov, A.; Artyushkova, K.; Atanassov, P.; Aricò, A.S.; Baglio, V. Performance, methanol tolerance and stability of Fe-aminobenzimidazole derived catalyst for direct methanol fuel cells. *J. Power Sources* **2016**, *319*, 235–246. [CrossRef]
72. Yang, X.; Xia, D.; Kang, Y.; Du, H.; Kang, F.; Gan, L.; Li, J. Unveiling the Axial Hydroxyl Ligand on Fe-N_4-C Electrocatalysts and Its Impact on the pH-Dependent Oxygen Reduction Activities and Poisoning Kinetics. *Adv. Sci.* **2020**, *7*, 2000176. [CrossRef]
73. Svane, K.L.; Reda, M.; Vegge, T.; Hansen, H.A. Improving the Activity of M−N 4 Catalysts for the Oxygen Reduction Reaction by Electrolyte Adsorption. *ChemSusChem* **2019**, *12*, 5133–5141. [CrossRef] [PubMed]
74. Fu, M.; Liu, Y.; Zhang, Q.; Ning, G.; Fan, X.; Wang, H.; Lu, H.; Zhang, Y.; Wang, H. Fe_2O_3 and Co bimetallic decorated nitrogen doped graphene nanomaterial for effective electrochemical water split hydrogen evolution reaction. *J. Electroanal. Chem.* **2019**, *849*. [CrossRef]
75. Fu, M.; Zhang, Q.; Sun, Y.; Ning, G.; Fan, X.; Wang, H.; Lu, H.; Zhang, Y.; Wang, H. Ni–Fe nanocubes embedded with Pt nanoparticles for hydrogen and oxygen evolution reactions. *Int. J. Hydrogen Energy* **2020**, *45*, 20832–20842. [CrossRef]
76. Song, C.; Wu, S.; Shen, X.; Miao, X.; Ji, Z.; Yuan, A.; Xu, K.; Liu, M.; Xie, X.; Kong, L.; et al. Metal-organic framework derived Fe/Fe3C@N-doped-carbon porous hierarchical polyhedrons as bifunctional electrocatalysts for hydrogen evolution and oxygen-reduction reactions. *J. Colloid Interface Sci.* **2018**, *524*, 93–101. [CrossRef]
77. Bagger, A.; Ju, W.; Varela, A.S.; Strasser, P.; Rossmeisl, J. Single site porphyrine-like structures advantages over metals for selective electrochemical CO_2 reduction. *Catal. Today* **2017**, *288*, 74–78. [CrossRef]
78. Zhou, Q.-S.; Peng, X.-W.; Zhong, L.-X.; Sun, R.-C. $CoSe_2$ nanobelt coupled with CoMoO4 nanosheet as efficient electrocatalysts for hydrogen and oxygen evolution reaction. *Environ. Sci. Ecotechnol.* **2020**, *1*, 100004. [CrossRef]
79. Jiang, J.; Chen, Y.; Cong, H.; Tang, J.; Sun, Y.; Hu, X.; Wang, L.; Han, S.; Lin, H. Highly efficient hydrogen evolution reaction of Co3O4 supports on N-doped carbon nanotubes in an alkaline solution. *Ionics* **2020**, *26*, 3437–3446. [CrossRef]
80. Zhang, Z.; Cong, L.; Yu, Z.; Qu, L.; Huang, W. Facile synthesis of Fe–Ni bimetallic N-doped carbon framework for efficient electrochemical hydrogen evolution reaction. *Mater. Today Energy* **2020**, *16*, 100387. [CrossRef]
81. Hou, D.; Zhang, J.; Li, Q.; Zhang, P.-F.; Chen, C.; Yan, D.; Mai, Y. Mesoporous Mo_2C/Carbon Hybrid Nanotubes Synthesized by a Dual-Template Self-Assembly Approach for an Efficient Hydrogen Production Electrocatalyst. *Langmuir* **2018**, *34*, 10924–10931. [CrossRef] [PubMed]
82. Liang, H.-W.; Brüller, S.; Dong, R.; Zhang, J.; Feng, X.; Müllen, K. Molecular metal–Nx centres in porous carbon for electrocatalytic hydrogen evolution. *Nat. Commun.* **2015**, *6*, 7992. [CrossRef] [PubMed]
83. Rheinländer, P.J.; Herranz, J.; Durst, J.; Gasteiger, H. Kinetics of the Hydrogen Oxidation/Evolution Reaction on Polycrystalline Platinum in Alkaline Electrolyte Reaction Order with Respect to Hydrogen Pressure. *J. Electrochem. Soc.* **2014**, *161*, F1448–F1457. [CrossRef]
84. Chao, S.; Xia, Q.; Wang, G.; Zhang, X. Fe_2O_3 nanoparticles immobilized on N and S codoped C as an efficient multifunctional catalyst for oxygen reduction reaction and overall water electrolysis. *Int. J. Hydrogen Energy* **2019**, *44*, 4707–4715. [CrossRef]
85. Lin, T.-W.; Liu, C.-J.; Dai, C.-S. Ni_3S_2/carbon nanotube nanocomposite as electrode material for hydrogen evolution reaction in alkaline electrolyte and enzyme-free glucose detection. *Appl. Catal. B Environ.* **2014**, *154-155*, 213–220. [CrossRef]
86. Sun, H.; Nie, M.; Xue, Z.; Luo, J.; Tang, Y.; Li, Q.; Teng, L.; Gao, T.; Xu, K. Study on the simple synthesis and hydrogen evolution reaction of nanosized ZnO coated MoS2. *Mater. Chem. Phys.* **2021**, *262*, 124279. [CrossRef]
87. Jaouen, F.; Marcotte, S.; Dodelet, J.-P.; Lindbergh, G. Oxygen Reduction Catalysts for Polymer Electrolyte Fuel Cells from the Pyrolysis of Iron Acetate Adsorbed on Various Carbon Supports. *J. Phys. Chem. B* **2003**, *107*, 1376–1386. [CrossRef]
88. Jaouen, F.; Lefèvre, M.; Dodelet, J.-P.; Cai, M. Heat-Treated Fe/N/C Catalysts for O_2 Electroreduction: Are Active Sites Hosted in Micropores? *J. Phys. Chem. B* **2006**, *110*, 5553–5558. [CrossRef]
89. Morozan, A.; Goellner, V.; Nedellec, Y.; Hannauer, J.; Jaouen, F. Effect of the Transition Metal on Metal–Nitrogen–Carbon Catalysts for the Hydrogen Evolution Reaction. *J. Electrochem. Soc.* **2015**, *162*, H719–H726. [CrossRef]
90. Barman, B.K.; Nanda, K.K. CoFe Nanoalloys Encapsulated in N-Doped Graphene Layers as a Pt-Free Multifunctional Robust Catalyst: Elucidating the Role of Co-Alloying and N-Doping. *ACS Sustain. Chem. Eng.* **2018**, *6*, 12736–12745. [CrossRef]

91. Paulus, U.A.; Schmidt, T.J.; Gasteiger, H.A.; Behm, R.J. Oxygen reduction on a high-surface area Pt/Vulcan carbon catalyst: A thin-film rotating ring-disk electrode study Oxygen reduction on a high-surface area Pt/Vulcan carbon catalysts: A thin-film rotating ring-disk electrode study. *J. Electroanal. Chem.* **2014**, *495*, 134–145. [CrossRef]
92. Ohma, A.; Shinohara, K.; Iiyama, A.; Yoshida, T.; Daimaru, A. Membrane and Catalyst Performance Targets for Automotive Fuel Cells by FCCJ Membrane, Catalyst, MEA WG. *ECS Trans.* **2011**, *41*, 775–784. [CrossRef]